공학박사학위논문

Crystallography of Martensitic transformation in TRIP steel & shape memory alloy

트립강과 형상기억합금에서 말텐사이트 변태의 결정학에 관한 연구

2017년 **8**월

서울대학교 대학원

재료공학부

김 양 후

Crystallography of Martensitic transformation in TRIP steel & shape memory alloy

트립강과 형상기억합금에서 말텐사이트 변태의 결정학에 관한 연구

지도교수 한 홍 남

이 논문을 공학박사학위논문으로 제출함
2017년 7월

서울대학교 대학원
재료공학부
김 양 후

김양후의 박사학위논문을 인준함
2017년 7월

위 원 장	박 은 수	(인)
부 위 원 장	한 홍 남	(인)
위 원	선 정 윤	(인)
위 원	서 동 우	(인)
위 원	Phaniraj Madakashira	(인)

ABSTRACT

Martensitic transformation (MT) in various metallic materials has been investigated for more than 100 years. Though great advances in the knowledge of martensite have been made by many researchers, fundamental understanding looks like being far away. Especially, complex microstructures of martensite in different alloys, which are the first subjects to catch up for comprehensive understanding of martensite and MT, are still puzzle. In a similar vein, the first and second parts of this thesis, respectively, deal with martensitic microstructures of the TRIP steel and Ti-based shape memory alloy (SMA) with crystallographic theories of MT. In the last part, as an effort to apply MT to real use, elastocaloric effect in V-added NiTi SMA was examined.

In first part, variant selection of mechanically induced MT in TRIP steel was investigated. A metastable austenite (γ) grain was nanoindented to introduce strain-induced MT, and multiple pop-ins, which imply transformation of the γ into martensite (α'), were detected in the nanoindentaion load-displacement curve. After the nanoindenation, cross-section of the indented region was observed using transmission electron microscope (TEM) equipped with an ASTAR system. Several martensite blocks with different variants maintaining the Kurdjumov-Sachs orientation relationship between the ex-

austenite within 5 degrees were confirmed. From a finite element calculation combined with phenomenological theory for MT, it was confirmed that each variants corresponded to those for which the transformation strain effectively accommodates external stress.

In second part, self-accommodation in Ti-V-Al SMA was studied. Exact phase information of the parent austenite and product martensite were extracted by Rietveld refinement using X-ray diffraction followed by microstructure observations using optic microscopy (OM), electron back scattered diffraction (EBSD) and TEM. The observed features of martensite microstructure including twinning mode of habit plane variants, invariant shear plane, variant clustering etc. were described with the geometrically nonlinear theory of martensite.

In third part, elastocaloric (EC) effect in polycrystalline Ni-Ti-V SMA alloy was examined. EC effect means thermal response of material respect to external uniaxial stress and have gathered much attention for the use of next-generation refrigeration systems, recently. By addition of a small amount of V (4.7 at.%), Ni-Ti-V SMA showed twice larger efficiency values such as EC cooling strength (= 50 °C GPa^{-1}) and coefficient of performance (= 22.5) than the conventional pure Ni-Ti. In addition to the efficiency improvements, the present alloy demonstrated the better functional fatigue property compared to

that of pure Ni-Ti. These result can be considered as a significant progress in finding suitable materials for an application of EC.

From the present study, crystallographic aspects of MT in TRIP and SMA are detailed and described well with solid theoretical backgrounds. Moreover, it is suggested that the newly developed alloy here can be a promising candidate for real application.

Keywords: Martensitic transformation (MT), TRIP steel, Shape memory alloy (SMA), Nanoindenation, Pop-in, Orientation relationship, Phenomenological theory of Martensitic transformation, Finite element method (FE), Transmission electron microscope (TEM), Variant selection, Electron back scattered diffraction (EBSD), Self-accommodation, Geometrical nonlinear theory of martensite, Elastocaloric effect (EC), Elastocaloric cooling strength, Coefficient of performance (COP), Functional fatigue

Student number: 2011-20630

Contents

Chapter 3

Self-accommodation of Ti–V–Al shape memory alloy

Chapter 4

Elastocaloric effect in polycrystalline $Ni_{50}Ti_{45.3}V_{4.7}$ shape memory alloy

Chapter 5

LIST OF TABLES

LIST OF FIGURES

of 0.025 s^{-1} and (b) the corresponding strength of EC effect $|\Delta T/\Delta\sigma|$.

Figure 4.6 (a) ΔT against the number of cycles during the fatigue test with a compressive stress of 260 MPa at a strain rate of 0.03 s^{-1}. (b) Compressive SS curve at a strain rate of 0.001 s^{-1} and (c) ΔT as a function of removed stress $\Delta\sigma$ at a strain rate of 0.025 s^{-1} after the mechanical training and fatigue test.

Chapter 1

Introduction

1.1 Martensitic transformation (MT)

Martensitic transformation (MT) in many alloys is a solid-solid diffusionless phase transformation in which transformation kinetics is independent on time term but determined by temperature and other mechanical conditions such as stress and strain. Generally, parent phase (high temperature stable) and product phase (low temperature stable) in MT are called as austenite and martensite, respectively, though they are originated from steel case. Compared to diffusional phase transform, MT shows several unique features below.

1. MT can be induced by different manners. Thermal quenching of austenite is the basic way to induce MT in most alloys [1]. However, other stimuli including mechanical stress/strain [2-5], ultra sound [6], and magnetic fields [7] also can be used to introduce MT in alloys.

2. MT is classified as reversible and irreversible transformation. In irreversible MT, for which MT in steel is a representative example, phase boundary between austenite and martensite is immobile and fixed once the

transformation occurred. In reversible MT, for which MT in shape memory alloy (SMA) is representative example, phase boundary is mobile that reverse transformation is possible under appropriate driving fields [8].

3. MT accompanies transformation strain originated from collective movement of atoms during the transformation. The transformation strain contains dilatation and shear components which are determined by the crystal structures and lattice parameters of the parent austenite and product martensite.

4. The feature 3 of MT implies that atomic movements for the transformation strain are occurred in deterministic manners. As a result, specific crystallographic orientation relationship (OR) is retained between two phases. For instance, Kurdjumov-Sachs OR in transformation between face centered cubic phase to body centered cubic or tetragonal [9] and Burgers OR in transformation between body centered cubic to hexagonal [10]. Besides, in accomplishing the transformation strain, there are several ways which yields equivalent strain in physical sense but distinguishable in crystallographic sense. The martensite formed by each way is called variant. Variant is minimum unit in martensite microstructure and specific variants are preferred, which is called variant selection, if MT occurs under certain conditions like external stress [11-15].

5. Martensite shows hierarchical microstructure consisted of clustered

variants. Generally, variants are formed to make twin structures, again, the twins are combined to form a specific ensemble attempt to minimize total shape change by MT. It is called self-accommodation [16-22]. Many self-accommodation microstructures including triangle [16,17], diamond [18,19] etc. are reported in various alloys.

1.2 Crystallographic theory of martensitic transformation

Theories for MT are classified by two classes. The first one is the phenomenological theory including WLR [23] and BM [24]. Though two theories are described by different mathematical formulations but yield the same result. Actually, Christian demonstrated that they are essentially equivalent in a rigorous manner [25]. The other one is the energy minimization theory by Ball and James in 1987 [26]. All these theories find the transformation strain and habit plane that assumed as an invariant plane using crystal structures and lattice parameters of the both phases considering the lattice correspondence. In addition, the two class yield similar result. Here, the energy minimization theory, also called as geometrically nonlinear theory, is briefly described.

To begin with, it is necessary to understand the concept of kinematic compatibility. The kinematic compatibility describes that the condition for continuous deformation of a body which suffers from different deformation gradients F_A and F_B as illustrated in figure 1.1. For keeping the continuity of the line at the interface of n, the following equation should be satisfied with a certain vector a.

$$F_A - F_B = a \otimes n \quad \cdots\cdots\cdots\cdots (1)$$

If any vector v which is lying on the interface is considered, it can be seen that

the kinematic compatibility is equivalent to the invariant plane condition as follows.

$$(F_A - F_B)v = (a \otimes n)v = a(v \cdot n) = 0 \quad \cdots\cdots\cdots\cdots (2)$$

In the microstructure of general shape memory alloys, finely twinned martensite variants forms the interface with austenite as shown in figure 1.2. Here, U_i and U_j are the transformation stretch matrices of i-th and j-th lattice correspondence variant which are determined by the lattice structures and parameters of austenite and martensite. The vectors n, a, m, b and f represent, respectively, twin plane normal, twin shear, phase interface normal, transformation shear and volume fraction of i-th variant. Firstly, the kinematic compatibility between the two martensite variants can be described as

$$RU_i - U_j = a \otimes n \quad \cdots\cdots\cdots\cdots (3)$$

where R is a certain rotation matrix. The eq. (3) is called twinning equation. Secondly, the kinematic compatibility between the austenite and two martensite variants is described as

$$R'(fRU_i + (1-f)U_j) - I = d \otimes m \quad \cdots\cdots\cdots\cdots (4)$$

where R' is also a certain rotation matrix which means the relative rotation between the two phases. The eq. (2) is called austenite-martensite interface equation. The procedure for finding solutions of eq. (2) and (3) requires several calculations steps, but explicit solutions according to the crystal systems of

austenite and martensite are can be found in the literatures [27-29].

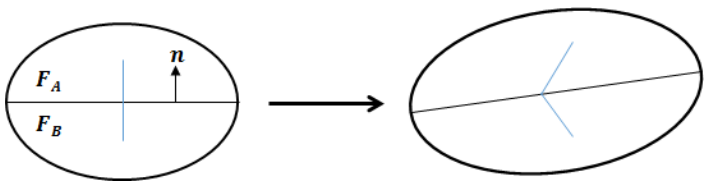

Figure 1.1 A body deforms by different deformation gradient F_A in the upper part and F_B in the lower part. The blue line keeps the continuity at the interface.

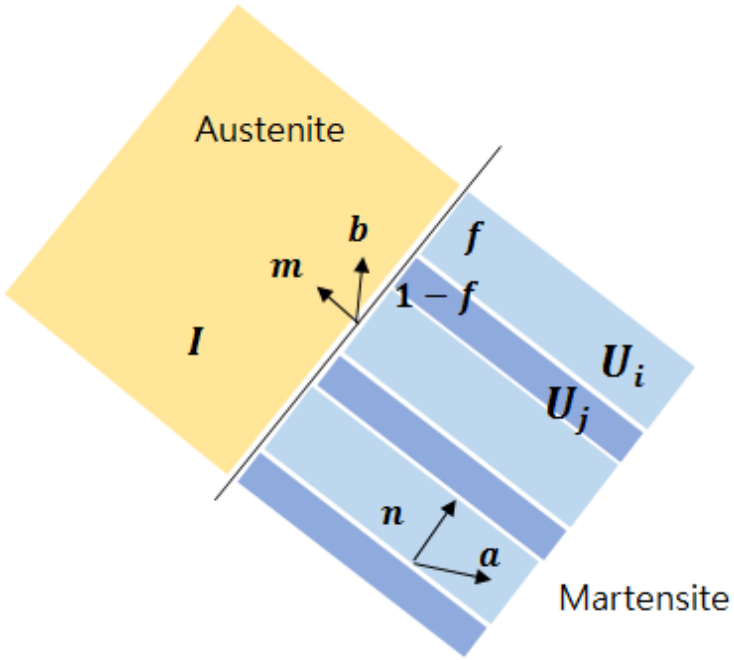

Figure 1.2 A schematic image of twined martensite variants and austenite.

1.3 References

[1] G.V. Kurdyumov, L.G. Khandros, Sov. Phys. Dokl. 66 (1949) 211.

[2] J.W. Christian, The Theory of Transformations in Metals and Alloys, Elsevier Science, Oxford (2002).

[3] Y. Kim, T-H. Ahn, D-W. Suh, H.N. Han, Scripta Mater. 104 (2015) 13.

[4] J. Talonen, P. Nenonen, G. Pape, H. Hanninen, Metal. Trans. A 36 (2005) 421.

[5] K. Spencer, M. Véron, K. Yu-Zhang, J. D. Embury, Mater. Sci. & Tech. 25 1 (2009) 7.

[6] V.V. Rubanik, V.V. Klubovich, Rubanik Jr., J. Phys. Ⅳ 112 (2003) 249.

[7] K. Inoue, K. Enami, Y. Yamaguchi, K. Ohoyama, Y. Morii, Y. Matsuoka, K. Inoue, J. Phys. Soc. Jpn. 69 (2000) 3485.

[8] J. Fernandez, X. M. Zhang, J. M. Guilemany, J. Mater. Porc. Tech. 139 (2003) 117.

[9] G. Kurdjumov, G. Sachs, Z. Phys. 64 (1930) 325.

[10] H. Beladi, Q. Chao, G. S. Rohrer, Acta Mater. 80 (2014) 478.

[11] J. R. Patel, M. Cohen, Acta Metall. 1 (1953) 531.

[12] S. Kundu, H.K.D.H. Bhadeshia, Scripta Mater. 55 (2006) 779.

[13] S. Kundu, H.K.D.H. Bhadeshia, Scripta Mater. 57 (2007) 869.

[14] E.S. Perdahcıoğlu, H. J. M. Geijselaers, Acta Mater. 60 (2012) 4409.

[15] B. Kim, T. T. T. Trang, N. J. Kim, Met. Mater. Int. 20 (2014) 35.

[16] S. Miyazaki, K. Otsuka, C. M. Wayman, Acta Metall. 37 (1989) 1873.

[17] K. Madangopal, Acta Mater. 45 (1997) 5347.

[18] T. Saburi, C. M. Wayman, K. Takata, S. Nenno, Acta Metall. 28 (1980) 15.

[19] J. X. Zhang, Y. F. Zheng, L. C. Zhao, Acta Mater. 47 (1999) 2125.

[20] T. Saburi, C. Wayman, Acta Metall. 27 (1979) 979.

[21] K. Adachi, J. Perkin, C. M. Wayman, Acta Metall. 34 (1986) 241.

[22] R.C. Pond, S. Celotto, J. P. Hirth, Acta Mater. 51 (2003) 5385.

[23] M.S. Wechsler, D.S. Lieberman, T.A. Read, Trans. AIME. 197 (1953) 1503.

[24] J.S. Bowles, J.K. Mackenzie, Acta Matall. 2 (1954) 129.

[25] J.W. Christian, J. Inst. Met. 84 (1955) 386.

[26] J. M. Ball and R. D. James, Arch. Rat. Mech. Anal. 100 (1987) 13.

[27] K. Bhattacharya, Microstructure of martensite, Oxford (2003).

[28] K. Bhattacharya, Conti. Mech. Thermo. 5 (1993) 205.

[29] K. F. Hane, T. W. Shield, J. of Elas. 59 (2000) 267.

Chapter 2

Variant selection during strain-induced martensitic transformation in TRIP steel

2.1 Introduction

The special crystal orientation relationship (OR) [1-3] between the parent austenite (γ) and the transformed phase is observed when martensite (α') or bainite structures are formed by displacive transformation. For example, the Kurdjumov-Sachs (KS) OR, consisting of 24 equivalent variants expressed as $\{111\}_{\gamma} \parallel \{011\}_{\alpha'}$, $\langle 101\rangle_{\gamma} \parallel \langle 111\rangle_{\alpha'}$, has been reported by many researchers [4-6]. In principle, the probability of selecting a variant from among 24 equivalent variants is identical, but under certain circumstances, such as in the presence of external stress, specific variants can be preferred.

Martensitic transformation, which occurs under external stress, has long been studied [7-11]. Patel and Cohen [7] discussed the effect of mechanical work by external stress on the martensite starting temperature. Kundu and Bhadeshia [8,9] showed that possible orientations of transformed α' can be predicted by considering the interaction energy associated with the transformation. Recently, Perdahcıoğlu et al. [10] considered the mechanical driving force in simulation of mechanically induced martensitic

transformation (MIMT) in stainless steel. However, there are few studies of MIMT under inhomogeneous external stress at a single-grain level.

The authors had suggested that the pop-in event observed on the load–displacement curve during nanoindentation of metastable austenite grain corresponds to the onset of MIMT [11]. In this paper, a multiple pop-in phenomenon, which is attributed to MIMT from metastable γ grain to several α' blocks during nanoindentation, was presented. The crystal OR between the two phases and variant selection during the transformation were quantitatively investigated by an automotive mapping technique with transmission electron microscope (TEM). The interaction energy between the applied stress and the transformation strain was evaluated by means of a finite element (FE) simulation and a phenomenological theory of martensitic transformation (PTMT).

2.2 Experimental procedure

TRIP steel with a chemical composition of Fe-0.08C-0.5Si-1Al-7Mn (wt.%) was used in the present work. A sequential procedure was carried out as follows [12,13].

1. Phase mapping of a polished surface using electron backscattered diffraction (EBSD; SU-70, Hitachi).
2. Nanoindentation (Hysitron) of individual γ grain using Berkovich tip with constant loading rate of 200 μN/s up to 1000 μN.
3. Cutting out of the cross-section of the indented region using a focused ion beam.
4. Confirmation of the phase formation using a transmission electron microscope (TEM) with crystallographic orientation and phase mapping by nanobeam diffraction in scanning mode using a TEM equipped with a NanoMEGAS ASTAR system.

The schematic diagram of above procedure is shown in figure 2.1.

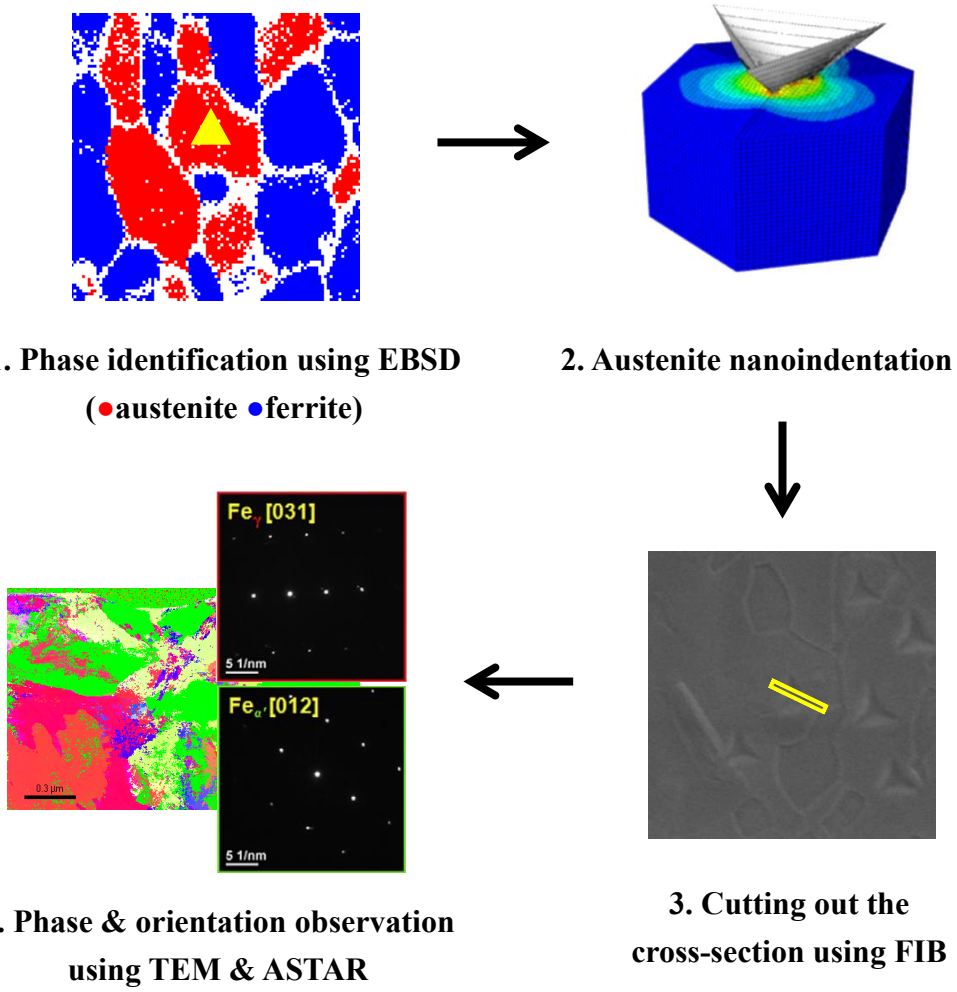

Figure 2.1 Schematic diagram of the sequential procedure carried out in the present study.

2.3 Variant selection during Strain-induced martensitic transformation by nanoindentation

Figure 2.2 shows the nanoindentation load-displacement curve of the indented γ grain. The blue broken line represents the Hertzian elastic contact solution [14], which was calculated with indenter tip radius of 400nm determined from a calibration using standard fused silica. There are several discontinuous displacement bursts. The first pop-in event is likely the result of dislocation nucleation in the annealed austenite grain based on the deviation from the Hertzian solution. The other pop-ins might be caused by strain-induced phase transformation from the parent γ to the transformed α'. This type of pop-in event had been detected and described as resulting from geometrical softening due to the selection of a favorable martensite variant [12]. Therefore, the multiple pop-in implies that the prior γ grain is transformed gradually as indentation proceeds. Figure 2.3 and Figures 2.4 (a) and (b) respectively show bright-field image and selected area diffraction pattern of each γ and α', phase and orientation maps in the normal direction of the cross-section of the indented region. The rectangular white broken line on Figure 2.3 corresponds to the frame of Figures 2.4 (a) and (b). The black lines represent the grain boundary or the phase interface when the misorientation angle exceeds 15°. With a partial volume of untransformed γ, the rest of prior austenite grain was transformed to several α' blocks, extended from the grain

boundary or free surface to the phase interface between the remaining γ.

Seven blocks of α' phase, M1 to M7, with a clear phase interface with the remaining γ, were identified based on the high angle boundary as shown in Figure 2.4 (a). Note that small blocks consisting of less than 20 pixels were excluded. In this study, the KS OR was considered adopting the sequence suggested by Takayama et. al [15] shown in table 2.1. The misorientation angles between the ideal KS OR and the experimental OR were calculated from the deviation matrix D^k, which is described as follows [16]:

$$D^k = M_{KS}^k \left(S^i g_A\right) \left(S^j g_M\right)^{-1} \quad (1)$$

Here, M_{KS}^k, g_A, g_M, S^i and S^j are the matrices which represent the k-th variant of the KS OR, the γ orientation, the α' orientation, and i-th and j-th symmetric operator in cubic system, respectively. The variant with the smallest misorientation angle θ was then determined. It can be written as follows:

$$\min_k \theta = cos^{-1}\left(\frac{tr(D^k)-1}{2}\right) \quad (2)$$

The calculations above were performed for all the pixels within each defined α' block, and the mean orientation of γ was used for g_A.

The determined KS OR variants and corresponding close-packed plane (CP) groups, Bain groups and mean misorientation angles for M1~M7 blocks are shown in Table 2. M1~M4, which belong to the same CP group, i.e., CP4, form a packet altering the Bain group between neighboring blocks. M1 consists of the V20/V23 variant pair, equivalent to V1/V4, in which the rotation axis

and angle are respectively [0 0.71 0.71] and 10.5 °. The OR between M3 and M4 is equivalent to that between V1 and V2, which the corresponding rotation axis and angle are [0.58 -0.58 0.58] and 60 °. The mean misorientation angles tend to become larger as the α' block is positioned closer to the indented surface. It is likely that the blocks near the indenter, subject to a relatively large amount of stress, are transformed earlier and that the subsequent deformation increases the misorientation. This is consistent with the sequential formation of α' blocks related to the multiple pop-ins as mentioned earlier.

The mechanical interaction energy U of martensitic transformation under external stress can be expressed as follows [17-19]

$$U = \frac{1}{2}\,\sigma_{ij}\varepsilon_{ij}^{TR} \qquad (3)$$

where σ_{ij} and ε_{ij}^{TR} are the symmetric stress and the transformation strain by applying symmetric operator to the shape deformation F, respectively, in the austenite coordinate system.

$$\varepsilon_{ij}^{TR} = sym\,(F - I) = \frac{1}{2}(F + F^{T}) - I \qquad (4)$$

The shape deformation F can be calculated using the PTMT [20,21]. In the Wechsler-Lieberman-Read (WLR) theory, single crystal austenite is assumed to be transformed into two parts of a banded structure, for which each volume fraction x_i is deformed by different Bain deformations B and rotations R.

$$F = x_1 R_1 B_1 + x_2 R_2 B_2, \quad x_1 + x_2 = 1 \qquad (5)$$

The alternative expression of eq (5), more frequently used, can be used here as

well

$$F = RGB \qquad (6)$$

Here, G denotes the lattice invariant shear deformation. The two relative orientations between the initial and the transformed phases can be calculated from the rotation, the Bain deformation and the axis relationships. Generally, the OR from the PTMT is irrational but close to the KS OR with a small misorientation angle. Crystallographic features of martensitic transformation such as the invariant shear plane, the shear direction and the amount of shear are also calculated as a function of the lattice parameters of both phases.

To determine the stress field σ_{ij} in the γ grain, an FE simulation for nanoindentation was performed using the commercial software ABAQUS (Ver. 6.10). It is difficult to determine the exact three-dimensional morphology of the indented γ and surrounding grains: thus, it was assumed that two hexahedral bodies with a trapezoidal base corresponding to the initial γ and α grains form a tilted phase interface, as shown in Figure 2.5. To consider the anisotropy, different elastic constants and orientations were used at each volume element. Also, volume expansion and a hardening effect in the partial γ volume due to the phase transformation were included. The elastic constants, (c_{11}, c_{12}, c_{44}), used for γ, α and α' were (154.0, 122.0, 77.0), (232.2, 135.6, 117.0) and (267.9, 110.8, 78.8) GPa, respectively [22-24]. The indenter tip was given as a rigid body sphere as shown in Figure 2.5. Though a Berkovich tip was used for the

actual indentation, it is reasonable that the tip is regarded as a sphere at a small depth, or near the onset of plastic deformation.

Figure 2.5 shows contour plots of normal and shear stress components on the cross-section of the used FE meshes in the deformed configuration. To estimate the interaction energy of the transformation, 24 transformation strains from the PTMT and the stress components from the FE simulation were inserted to Eq. (3). The calculated interaction energies with positive values for each transformation strain and the corresponding KS variants in M1 and M2 are listed in Table 3. For convenience, the OR from the PTMT was assumed to be the exact KS OR in identifying the variant. The interaction energy can be considered as the driving force of the transformation. Therefore, variants with a large amount of positive interaction energy are more likely to become activated during the transformation. In that sense, as listed in Table 2, it is notable that V23 and V19, the KS variants of M1 and M2, respectively, have the highest interaction energy.

Table 2.1 24 variants of the KS OR.

Variant #	Plane parallel	Direction parallel
V1	$(111)_\gamma$ // $(011)_\alpha$	$[-101]_\gamma$ // $[-1-11]_\alpha$
V2		$[-101]_\gamma$ // $[-11-1]_\alpha$
V3		$[01-1]_\gamma$ // $[-1-11]_\alpha$
V4		$[01-1]_\gamma$ // $[-11-1]_\alpha$
V5		$[1-10]_\gamma$ // $[-1-11]_\alpha$
V6		$[1-10]_\gamma$ // $[-11-1]_\alpha$
V7	$(1-11)_\gamma$ // $(011)_\alpha$	$[10-1]_\gamma$ // $[-1-11]_\alpha$
V8		$[10-1]_\gamma$ // $[-11-1]_\alpha$
V9		$[-1-10]_\gamma$ // $[-1-11]_\alpha$
V10		$[-1-10]_\gamma$ // $[-11-1]_\alpha$
V11		$[011]_\gamma$ // $[-1-11]_\alpha$
V12		$[011]_\gamma$ // $[-11-1]_\alpha$
V13	$(-111)_\gamma$ // $(011)_\alpha$	$[0-11]_\gamma$ // $[-1-11]_\alpha$
V14		$[0-11]_\gamma$ // $[-11-1]_\alpha$
V15		$[-10-1]_\gamma$ // $[-1-11]_\alpha$
V16		$[-10-1]_\gamma$ // $[-11-1]_\alpha$
V17		$[110]_\gamma$ // $[-1-11]_\alpha$
V18		$[110]_\gamma$ // $[-11-1]_\alpha$
V19	$(11-1)_\gamma$ // $(011)_\alpha$	$[-110]_\gamma$ // $[-1-11]_\alpha$
V20		$[-110]_\gamma$ // $[-11-1]_\alpha$
V21		$[0-1-1]_\gamma$ // $[-1-11]_\alpha$
V22		$[0-1-1]_\gamma$ // $[-11-1]_\alpha$
V23		$[101]_\gamma$ // $[-1-11]_\alpha$
V24		$[101]_\gamma$ // $[-11-1]_\alpha$

Table 2.2 KS OR variants, CP groups, Bain groups and misorientation angles of M1~M7.

Block	Variant #	CP	Bain	Misorientation (degree)
M1	20+23	CP4	B2	4.9±1.3
M2	19	CP4	B3	2.7±1.1
M3	24	CP4	B1	1.2±0.4
M4	23	CP4	B2	1.1±0.5
M5	21	CP4	B1	3.5±0.5
M6	21	CP4	B1	3.5±0.6
M7	9	CP2	B3	2.7±0.8

Table 2.3 Calculated interaction energy of 24 transformation strains and corresponding KS variants in M1 and M2.

M1		M2	
Interaction Energy (J/mol)	Variant #	Interaction Energy (J/mol)	Variant #
295.3	***23***, 24	***322.9***	***19***, 20
287.9	15, 16	312.7	21, 22
198.4	19, 20	263.3	5, 6
184.1	17, 18	230.0	11, 12
147.2	1, 2	190.5	3, 4
146.5	23, 24	154.1	9, 10
142.6	15, 16	104.3	13, 14
141.0	7, 8	98.5	19, 20
124.9	5, 6	91.2	5, 6
111.7	9, 10	91.0	17, 18
		80.8	21, 22
		68.1	11, 12

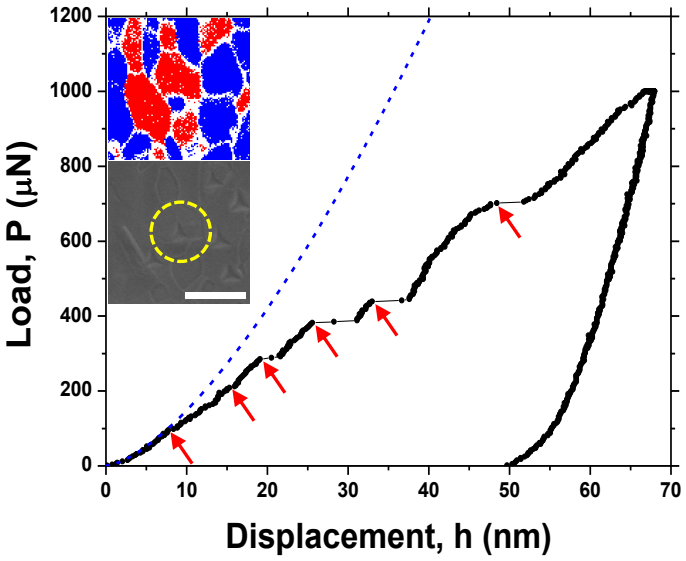

Figure 2.2 The nanoindentation load-displacement curve of the indented γ grain (yellow circle). The blue broken line represents the Hertzian elastic contact solution. Red arrows indicate the starting points of several pop-ins. The insets show a phase map (red: FCC γ, blue: BCC α' or ferrite (α)) of the indented surface and a scanning electron microscope image after indentation.

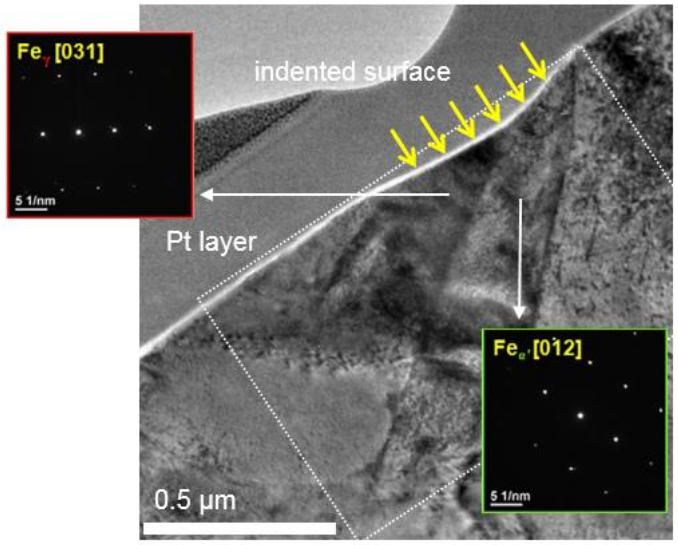

Figure 2.3 Bright-field image and SADP of γ and α' by TEM.

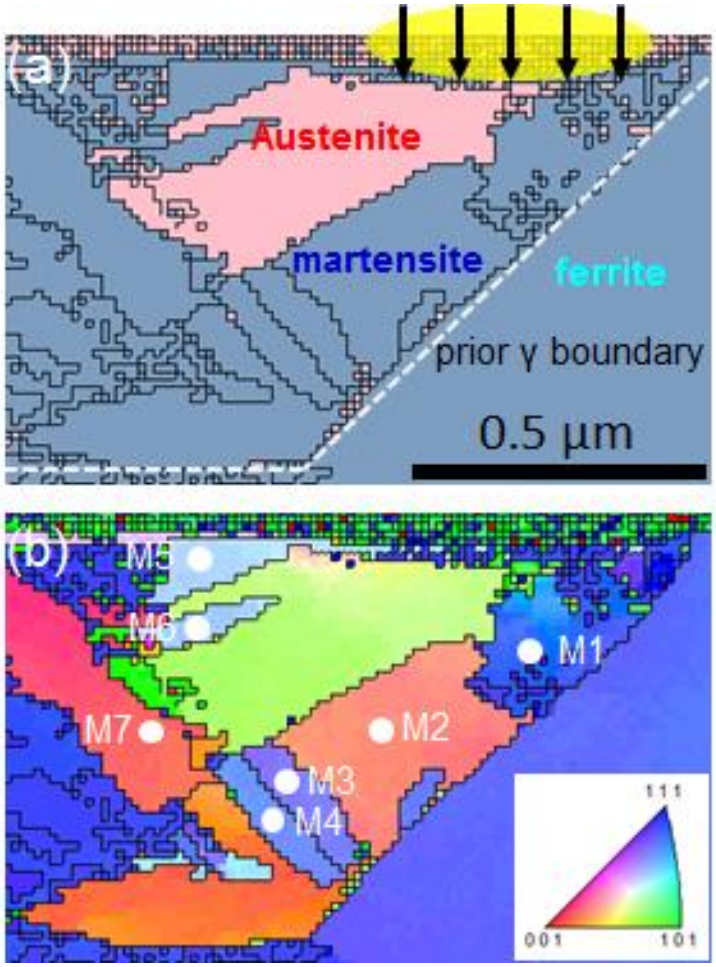

Figure 2.4 (a) Phase map (pink: FCC γ, steel blue: BCC α' or α) and (c) orientation map of the cross-section of the indented region from ASTAR in TEM. The black lines in (a) and (b) represent the grain boundary or phase interface when the misorientation angle exceeds 15°.

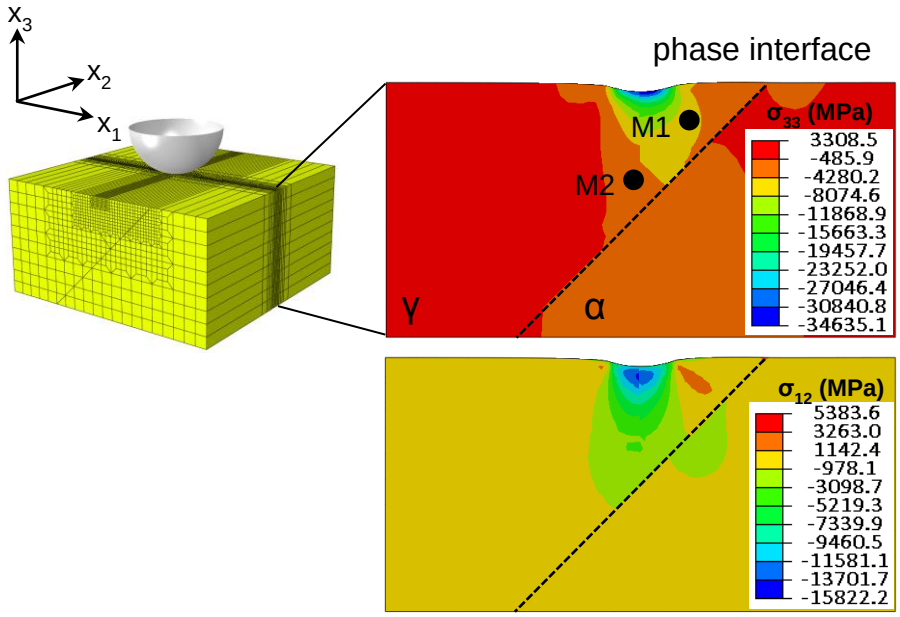

Figure 2.5 Used meshes in an FE simulation and cut-views of the distribution of the stress components σ_{33} and σ_{12} at indentation depth of 10nm.

2.4 Conclusion

Multiple pop-ins were observed during the nanoindentation of the γ grain in TRIP steel. ASTAR observations confirmed that the partial volume of the prior γ grain was transformed into several α' blocks with different variants. This is attributed to sequential martensitic transformation from metastable γ to α' under an inhomogeneous stress state. In addition, the interaction energy associated with the transformation was estimated using the FE simulation combined with the PTMT. It appeared that the interaction energy between the stress and the transformation strain plays an important role with regard to variant selection during MIMT.

2.5 References

[1] G. Kurdjumov, G. Sachs, Z. Phys. 64 (1930) 325.

[2] Z. Nishiyama, Sci. Rep. Tohoku Univ. 23 (1934) 637.

[3] A. B. Greninger, A. R. Troiano, Trans. AIME 185 (1949) 590.

[4] S. Morito, H. Tanaka, R. Konishi, T. Furuhara, T. Maki, Acta Mater. 51 (2003) 1789.

[5] H. N. Han, C. G. Lee, C.-S. Oh, T.-H. Lee and S.-J. Kim, Acta Mater. 52 (2004) 5203.

[6] S. Nambu, N. Shibuta, M. Ojima, J. Inoue, T. Koseki, H.K.D.H. Bhadeshia, Acta Mater. 61 (2013) 4831.

[7] J. R. Patel, M. Cohen, Acta Metall. 1 (1953) 531.

[8] S. Kundu, H.K.D.H. Bhadeshia, Scripta Mater. 55 (2006) 779.

[9] S. Kundu, H.K.D.H. Bhadeshia, Scripta Mater. 57 (2007) 869.

[10] E.S. Perdahcıoğlu, H. J. M. Geijselaers, Acta Mater. 60 (2012) 4409.

[11] B. Kim, T. T. T. Trang, N. J. Kim, Met. Mater. Int. 20 (2014) 35.

[12] T.-H. Ahn, C.-S. Oh, D.H. Kim, K.H. Oh, H. Bei, E.P. George, H.N. Han, Scripta Mater. 63 (2010) 540.

[13] T.-H. Ahn, S. B. Lee, K.-T. Park, K. H. Oh, H. N. Han, Mater. Sci. Eng. A 598 (2014) 56.

[14] K. L. Johnson, Contact Mechanics, London, UK: Cambridge University Press (1985).

[15] N. Takayama, G. Miyamoto, T. Furuhara, Acta Mater. 60 (2012) 2387.

[16] G. Miyamoto, N. Iwata, N. Takayama, T. Furuhara, Acta Mater. 58 (2010) 6393.

[17] M. Humbert, B. Petit, B. Bolle, N. Gey, Mater. Sci. Eng. A 454-455 (2007) 508.

[18] H.N. Han, D. W. Suh, Acta Mater. 51 (2003) 4907.

[19] S. H. Lee, J.-Y. Kang, H. N. Han, K. H. Oh, H.-C. Lee, D.-W. Suh, S.-J. Kim, ISIJ Int. 45 (2005) 1217

[20] M.S. Wechsler, D.S. Lieberman, T.A. Read, Trans. AIME. 197 (1953) 1503.

[21] J.S. Bowles, J.K. Mackenzie, Acta Matall. 2 (1954) 129.

[22] M. Humbert, B. Gardiola, C. Esling, G. Flemming, K.E. Hensger, Acta Mater. 50 (2002) 1741.

[23] Sudook A. Kim, Ward L. Johnson, Mater. Sci. Eng. A 452-453 (2007) 633.

[24] D.J. Dever, J. Appl. Phys. 43(8) (1972) 3293.

Chapter 3

Self-accommodation in Ti−V−Al shape memory alloy

3.1 Introduction

Martensite microstructure in various metallic materials has been a challenge for metallurgists for a long time. The martensite microstructure is formed by filling ex-austenite grain with different variants which are unique crystallographic set generated by crystalline symmetry of austenite and martensite. Generally, the variants tend to combine or arrange in special manner to minimize the macroscopic transformation strain and it is called as self-accommodation.

Up to now, many self-accommodation microstructures of martensite, especially in shape memory alloys (SMAs) which shows typical twinned structure, have been reported according to crystal structures of the parent and product phases and chemical composition of alloys. For examples, Saburi and Wayman showed that four habit plane variants (HPV) around {110} poles are clustered for reducing elastic stored energy in Cu-Zn-Al SMA [1]. And Murakami et al. also demonstrated that Ni-Al transformed from cubic to tetragonal crystal structure in the same way as Cu-Zn-Al for self-

accommodating structure [2]. In NiTi, V-shaped minimum units of two HPVs connected as {111} type I twin form to trianglur, rhombic and hexangular self-accommdationg shapes [3-6]. In addition, investigations on self-accommodation in cubic to orthorhombic martensitic transformation (MT), such as Ti-Nb have been reported. [7-8].

Compared to the conventional SMA NiTi, Ti-based SMA has many advantages including formability, biocompatibility and high transformation temperature [9-10]. Among Ti-based SMA, Ti-V-Al have appeared as a promising candidate due to its lightweight property [11-15]. The third element Al acts as an α" stabilizer as well as suppress ω phase which lower the phase transformation temperature [16-17]. However, little systematic research on microstructure or self-accommodation has been reported. In this study, self-accommodation microstructure of Ti-V-Al SMA, which shows body centered cubic (β) to orthorhombic (α") MT, was detailed.

3.2 Experimental procedure

Ti−12.3V−(0,5)Al (at.%) alloys, named hereafter Al0 and Al5, respectively, were prepared by arc-melting from high purity elements under an Ar atmosphere. For chemical homogeneity, 7 cycles of flipping over – remelting were repeated. After homogenization at 1000 °C for 10 h, cold rolling with reduction ratio of 50% was carried out. And the rolled sheet was solution treated in a vacuum furnace at 1000 °C for 30 min followed by cold water quenching. The θ-2θ X-ray diffraction (XRD; D8-Advanced, Bruker) measurements were performed to extract the phase formation and lattice parameters of each phase with Cu $K\alpha_1$ radiation at a scanning rate of 1 degree/min.

The microstructure of Ti−12.3V−5Al, which is full α" martensite structure, was observed using optical microscope (OM), electron backscattered diffraction (EBSD) and transmission electron microscope (TEM). The sample for EBSD was prepared by mechanical polishing up to 1200 grit followed chemical etching in a solution of 2% HF, 5% HNO_3 and H_2O (vol. %) for 20 s. Accelerating voltage and probe current of were 20 kV and 4 nA, respectively, were used in EBSD measurement. The TEM sample was prepared by mechanical polishing up to a thickness of about 100 μm followed by twin-jet polishing with a solution containing 6 % perchloric acid, 34 % n-butanol and 60 % methanol (vol.%). TEM observation was carried out with a JEOL-2100F

at an accelerating voltage of 200 KV.

3.3 Self-accommodation microstructure

Figure 3.1 shows the XRD patterns at room temperature (RT). The blue lines reveals that the Al5 is consisted of full α" martensite which is orthorhombic crystal structure. Besides, the Al0 is consisted of both α" martensite and β austenite. These result implies that RT is between the martensite start and finsh temperature of the Al0 so that β→α" martensitic transformation was not completed during the quenching but partial fraction of β was transformed. For determining the lattice parameters of martensite, Reitveld refinement (red line) was performed using free software FULLPROF. The R_{wp}, R_{exp} and χ^2 which are the goodness values of the Reitveld refinement were 33.8, 22.0 and 2.36, respectively. The determined lattice parameters from the Reitveld refinement are shown in table 3.1. Note that lattice parameter of β was determined by Bragg's law due to the lack of diffraction picks.

Figures 3.2 shows the optical microscopy (OM) images of Al5 alloys at the magnifications of x1000. There is no evident self-accommodation morphology but V shape and triangular morphologies are dominantly observed. In addition, small zig-zag and parallel branches between two parallel branches can be observed.

After catching a big picture of the microstructure by OM, EBSD measurement was carried out. Figure 3.3 (a) and (b) show the image quality and orientation map in the normal direction of the observed area. It was assumed

that each branch has a fixed orientation from the fact that the orientation spread was less than 2.5° in all branches (figure 3.4) which are consisted of only 6 orientations labelled from 1 to 6.

Before the considering the orientation relationship (OR) between each branched, stereographic projection of [100] pole of each branch was drawn as shown in figure 3.5. It can be seen that three pairs in which two orientations are closely positioned are mutually perpendicular so each branch is correspond to lattice correspondence variant (LCV). From the <100> and {111} pole figures of each LCVs in figure 3.6, only one OR between the LCVs, {111} type I twin OR, was detected. For example, procedure of finding the OR between LCV2 and LCV5 was illustrated in figure 3.7. The coincident point of both {111} poles was found followed by proper rotation so that the coincident point moves to special position such as [010]. Then <100> poles of each LCV are in mirror position confirming that the coincident {111} plane is mirror plane. In the same manner, all possible (LCV_i, LCV_j) pairs except (LCV1, LCV2), (LCV3, LCV4), (LCV5, LCV6), which are impossible to make type I OR, were examined.

Figure 3.8 (a)-(e) show TEM bright field (BF) images and selected area diffraction patterns (SADP) of encircled area. From the 3.8 (a) and (b), it can be checked that each branch has a single orientation so that the assuming in analysis of EBSD data was reasonable. In addition, the {111} type I OR was reconfirmed. In the SADP of the boundary region of zig-zag branches, the {111} type I twin is evident as shown in the key diagram (Figure 3.8 (e)).

To describe the observed features of microstructure in the present alloy, the MT theory introduced in chapter 1.2 was adopted. Using the lattice parameters from the XRD data and Reitveld refinement, the twinning equation 1.2 (1) and austenite-martensite interface equation 1.2 (2) were numerically solved and the results are listed in table 3.2 and 3.3. In β→α" MT, three possible twinning mode, compound twin by (LCV1, LCV2), (LCV3, LCV4), (LCV5, LCV6) combinations, {111} type I twin and <211> type II twin by the other combinations, (LCVi, LCVj, i≠j+1), are possible if only kinematic compatibility between LCV combinations are considered. If the kinematic compatibility between parent austenite and finely twinned LCV combinations is considered simultaneously, only the {111} type I twin and <211> type II are possible as shown in table 3.3. Note that in a combination of two LCVs, four solutions are obtained. Comparing to the analysis of EBSD and TEM data, the fact that {111} type I twins were observed is agreement with the prediction of theory.

Let's turn to the aspect of self-accommodation in the present alloy. Here, the author assumes that real habit plane of twined LCVs follows the solution of MT theory mentioned above. In figure 3.9, 48 habit plane normals of LCVs combination calculated by MT theory were drawn as black circles in the stereographic projection. In addition, applying surface trace analysis, which uses the orthogonal property between the trace and normal directions of a plane,

possible habit plane traces of each twinned branch are drawn as straight lines. The red star represents the normal direction of observed area in EBSD. The solutions which is encircled as red and blue were selected as habit planes. Though the real habit plane of the present alloy should be unique, two solutions will be tested here. If we calculate cross product between the normal direction of observed area and selected habit plane normal, the traces of habit planes in the observed plane can be obtained as shown in figure 3.10. Now, the observed morphologies such as V, triangle and zig-zag shapes can be accounted by selecting two or three solutions as illustrated in figure 3.11.

It is necessary to evaluate the average shape strain when three habit planes form a triangle shape as a self-accommodation morphology. There are only two cases, combination (1,2,3) and (4,5,6). The average shape strain is defined as

$$E_{(ijk)} = (E_i + E_j + E_k)/3 \qquad \ldots\ldots (1)$$

where, E_i is the shape change of each calculated habit plane variant and only two case of (i,j,k), (1,2,3) and (4,5,6), are considered. In table 3.4, the calculated average shape strains and shape strain of single habit plane variant are listed. For clear comparison, the diagonalized $E_{(ijk)}$ and E_i are also calculated. Comparing the $E_{(ijk)}$ and E_i in (i,j,k)=(1,2,3) case, it is evident that when the habit plane variants make the triangle, the anisotropy of diagonal term of shape strain is released so that it can help to reduce the macroscopic shape change. in In (i,j,k)=(1,2,3) case, however, no significant effect on reducing the anisotropy by formation of triangular morphology. So it can be concluded that the real

habit plane is near the solution of red circle in figure 4.

Table 3.1 Lattice parameters of α” and β from Reitveld refinement.

Phase	**Martensite (α”)**	**Austenite (β)**
Space group	C m c m	I m -3 m
Lattice parameter (Å)	a= 2.9745 b= 4.9470 c = 4.6364	a0= 3.2458

Table 3.2 LCV combinations and corresponding twinning mode predicted by twinning equation.

$\downarrow U_j$ \ $\rightarrow U_i$	CV1	CV2	CV3	CV4	CV5	CV6
CV1		C $(011)_M$ C $(01\text{-}1)_M$	Ⅰ $(1\text{-}11)_M$ Ⅱ $[2\text{-}11]_M$	Ⅰ $(11\text{-}1)_M$ Ⅱ $[21\text{-}1]_M$	Ⅰ $(\text{-}111)_M$ Ⅱ $[\text{-}211]_M$	Ⅰ $(111)_M$ Ⅱ $[211]_M$
CV2			Ⅰ $(\text{-}111)_M$ Ⅱ $[\text{-}211]_M$	Ⅰ $(111)_M$ Ⅱ $[211]_M$	Ⅰ $(11\text{-}1)_M$ Ⅱ $[21\text{-}1]_M$	Ⅰ $(1\text{-}11)_M$ Ⅱ $[2\text{-}11]_M$
CV3				C $(01\text{-}1)_M$ C $(011)_M$	Ⅰ $(1\text{-}11)_M$ Ⅱ $[2\text{-}11]_M$	Ⅰ $(11\text{-}1)_M$ Ⅱ $[21\text{-}1]_M$
CV4					Ⅰ $(\text{-}111)_M$ Ⅱ $[\text{-}211]_M$	Ⅰ $(111)_M$ Ⅱ $[211]_M$
CV5						C $(011)_M$ C $(01\text{-}1)_M$
CV6						

C = compound twin, Ⅰ = type Ⅰ twin, Ⅱ = type Ⅱ twin

Table 3.3 Solutions of austenite-martensite interface equation.

	CV pairs	f	Habit plane
type Ⅰ	(1,3),(1,4),(1,5),(1,6) (2,3),(2,4),(2,5),(2,6) (3,4),(3,5),(3,6),(4,5) (4,6)	0.2127	$\boldsymbol{b}$= <0.0843,0.0472,0.0817> <0.0967,0.0447,0.0684> $\boldsymbol{m}$= {0.7215,0.3763,0.5813} {0.7215,0.3763,0.5813}
type Ⅱ		0.2476	$\boldsymbol{b}$= < 0.0793,0.0318,0.0802> < 0.0865,0.0467,0.0636> $\boldsymbol{m}$= {0.6992,0.4142,0.5827} {0.6334,0.2942,0.7157}

Table 3.4 Calculated the average shape strain, E_{ijk}, and shape strain of single habit plane variant, E_i. The corresponding diagonalized matrix is written just below.

	E_{ijk}	E_i
123	0.9761 -0.0011 0.0487 -0.0036 0.9883 0.0305 -0.0184 0.0013 1.0332	0.9427 0.0262 0.0590 -0.0293 1.0134 0.0302 -0.0403 0.0184 1.0415
	1.0418 0.0000 0.0000 0.0000 0.9705 0.0000 0.0000 0.0000 0.9866	0.9432 0.0000 0.0000 0.0000 1.0000 0.0000 0.0000 0.0000 1.0576
456	1.0144 -0.0287 0.0294 0.0298 0.9414 0.0600 0.0207 -0.0407 1.0417	1.0134 -0.0293 0.0302 0.0262 0.9427 0.0590 0.0184 -0.0403 1.0415
	1.0589 0.0000 0.0000 0.0000 0.9999 0.0000 0.0000 0.0000 0.9421	1.0576 0.0000 0.0000 0.0000 1.0000 0.0000 0.0000 0.0000 0.9432

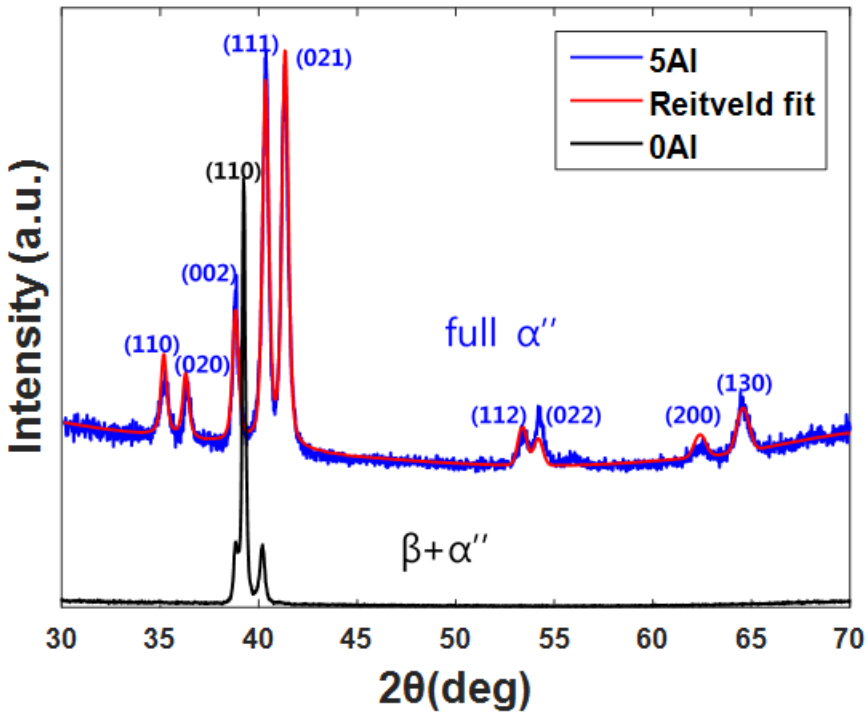

Figure 3.1 XRD patterns and Reitveld refinement fitting at RT.

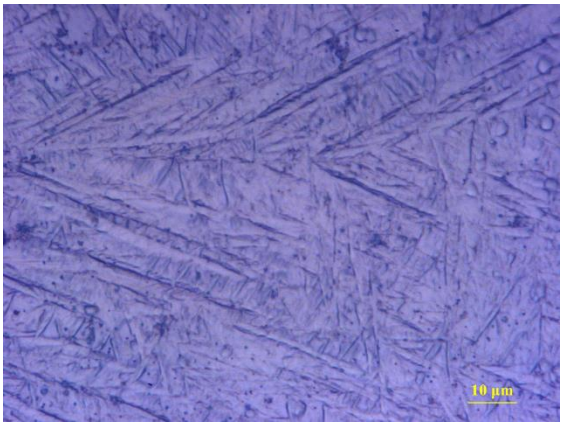

Figure 3.2 OM images of Al5 at the magnifications of x1000.

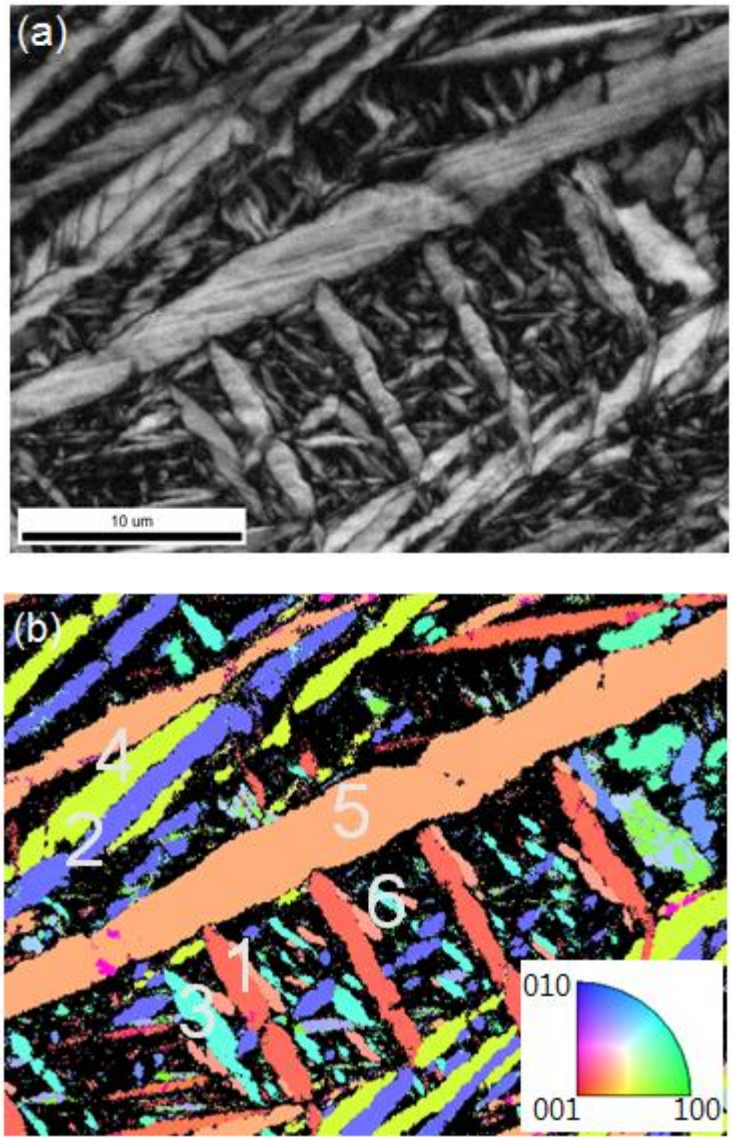

Figure 3.3 (a) EBSD image quality and (b) orientation map in the z direction.

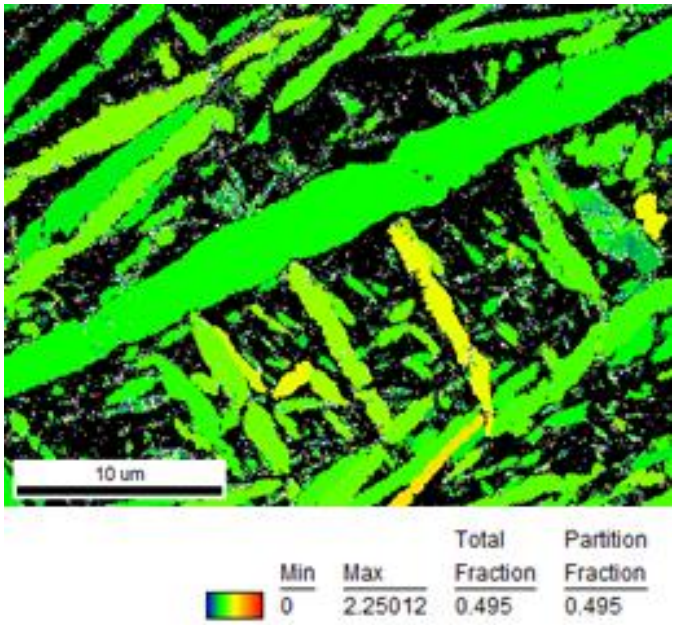

Figure 3.4 Grain orientation spread map of observed area by EBSD.

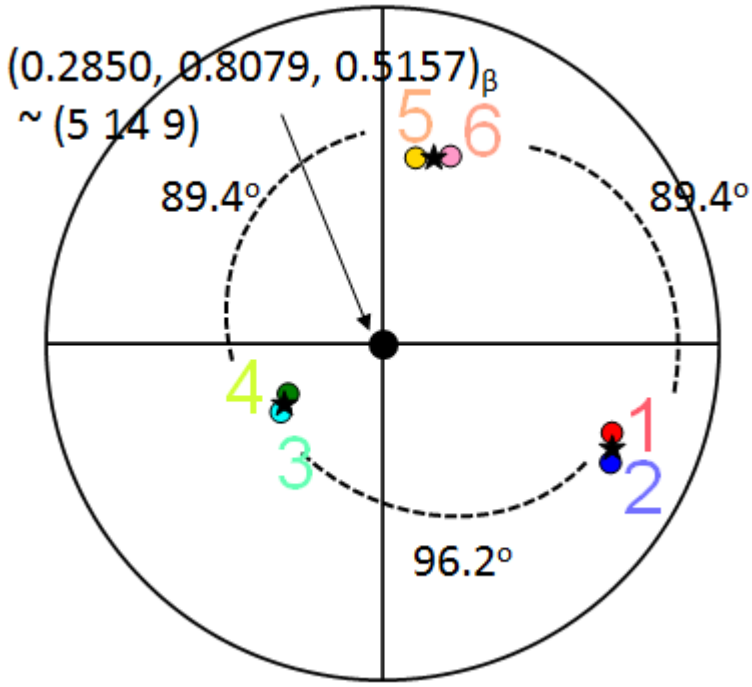

Figure 3.5 Stereographic projection of [100] poles of each branch.

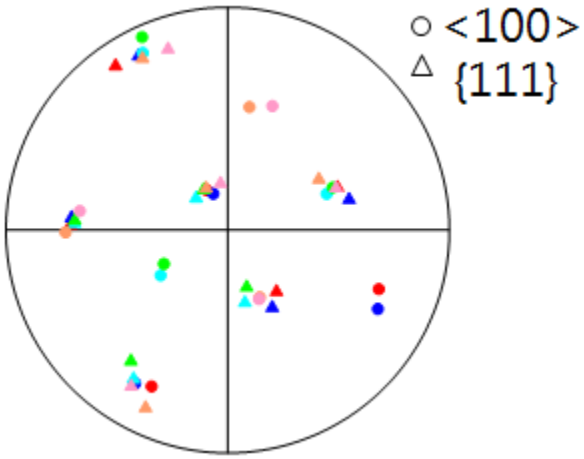

Figure 3.6 <100> and {111} pole figures of all LCVs.

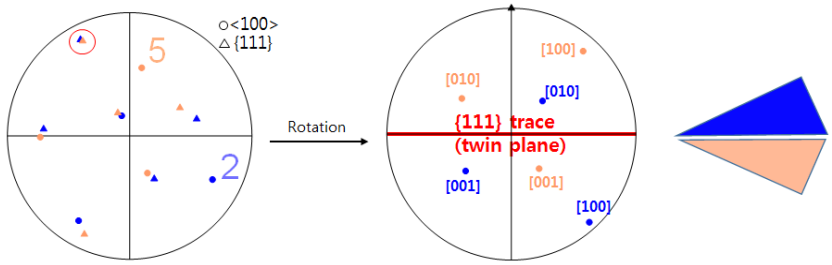

Figure 3.7 Schematic illustration of procedure for checking the OR of {111} type I twin.

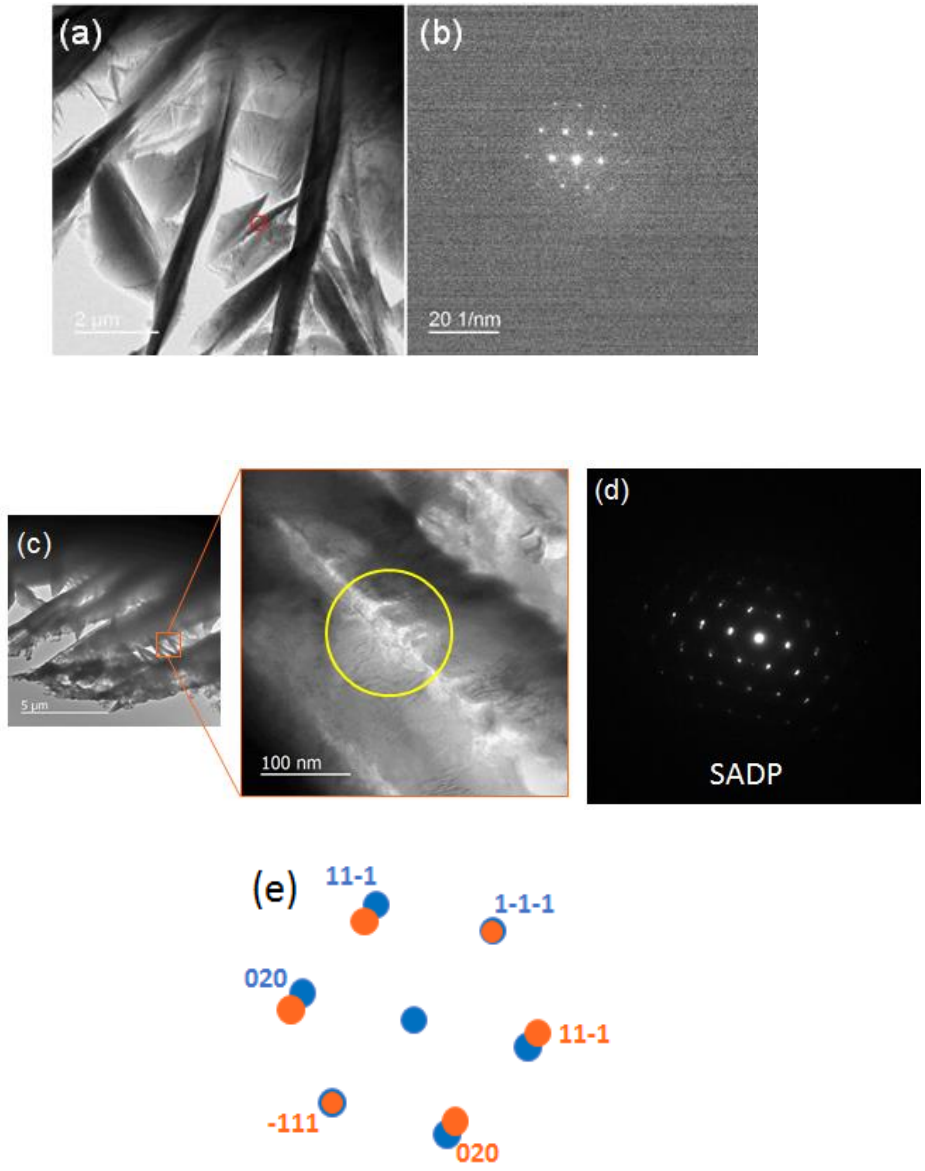

Figure 3.8 (a)-(d) TEM BF images and SADP of encircled area (e) key diagram of (d).

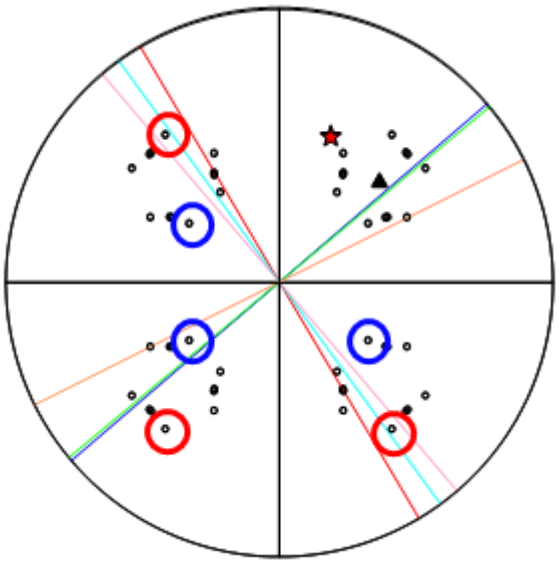

Figure 3.9 Habit plane traces (lines) of each LCV by surface trace analysis and habit plane poles (black circles) predicted by theory.

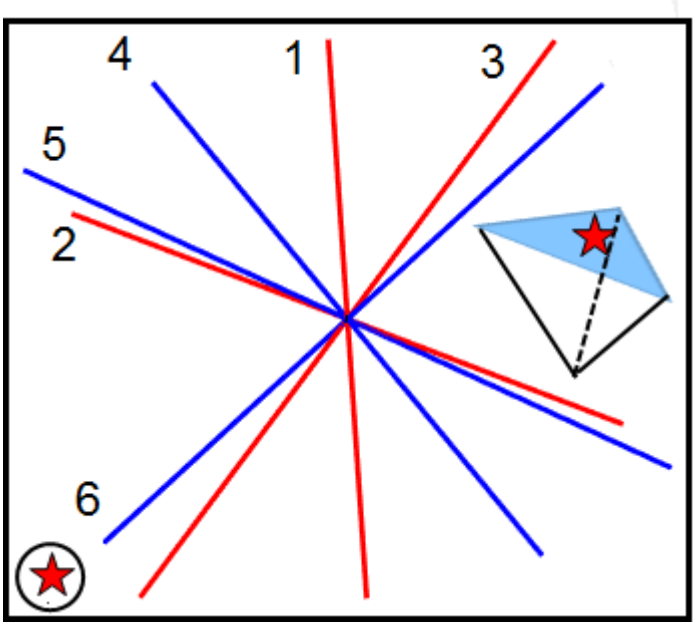

Figure 3.10 Possible habit plane traces by selected solutions in the observed plane of EBSD.

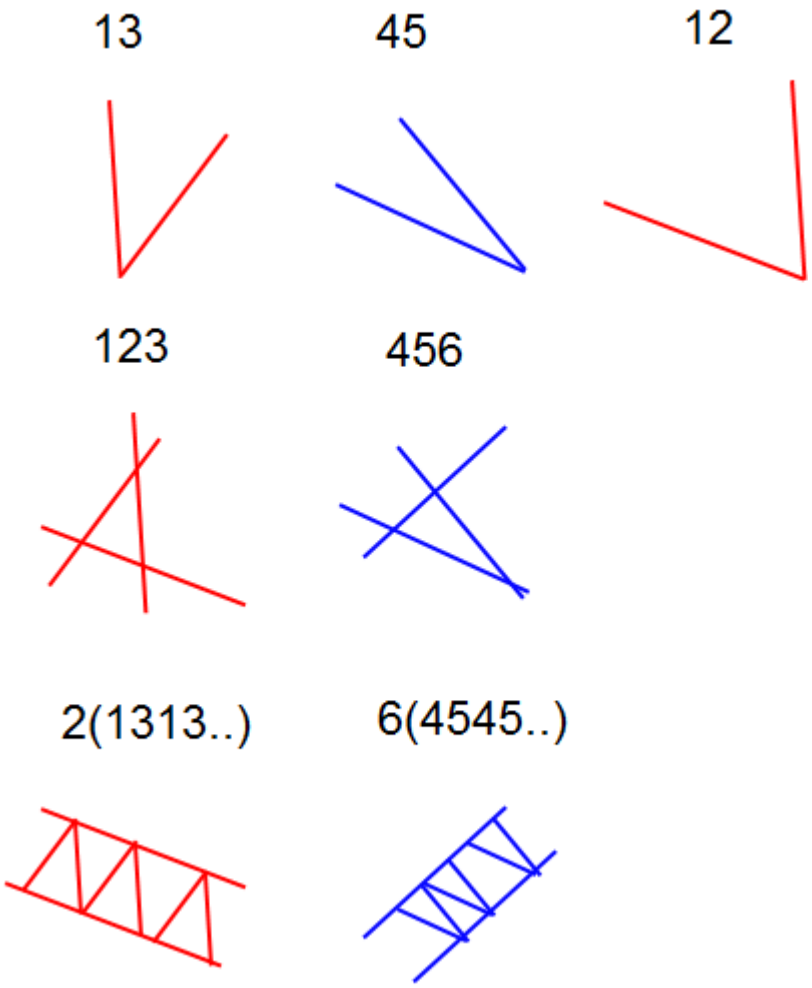

Figure 3.11 Possible habit plane combinations and corresponding traces by two for V shape, three for triangle and variation of three for zig-zag.

3.4 Conclusion

Self-accommodation microstructure of Ti-V-Al was investigated using OM, EBSD and TEM observation. The exact unit cell structure including space group and lattice parameters and atomic positions of orthorhombic α" martensite were extracted by Reitveld refinement of XRD. From the orientation information of EBSD and TEM, {111} type I twins are mainly observed which can be explained by MT theory. From the surface trace analysis combined with MT theory, the trace morphologies like V, triangular and zig-zag shape was explained. In addition, the triangular morphology, which can reduce the degree of anisotropy in axial strain components, was confirmed as self-accommodation microstructure in Ti-V-Al SMA.

3.5 References

[1] T. Saburi and C. M. Wayman, Acta Metall 27 (1979) 979.

[2] Y. Myrakami, K.Otuska, S. Hanada, S. Watanabe, Mater. Sci. Eng. A 189 (1994) 191.

[3] M. Nishida, T. Nishiura, H. Kawano, T. Inamura, Phil. Mag 92 17 (2012) 2215.

[4] M. Nishida, E. Okunishi, T. Nishiura, H. Kawano, T. Inamura, S. Ii, T. Hara, Phil. Mag 92 17 (2012) 2234.

[5] T. Inamura, T. Nishiura, H. Kawano, H. Hosoda, M. Nishida, Phil. Mag 92 17 (2012) 2247.

[6] Y. Soejima, S. Motomura, M. Mitsuhara, T. Inamura, M. Nishida, Acta Mater 103 (2016) 352.

[7] Y. W. Chai, H. Y. Kim, H. Hosoda, M. Miyazaki, Acta Mater 57 (2009) 4054.

[8] Y. W. Chai, H. Y. Kim, H. Hosoda, M. Miyazaki, Acta Mater 56 (2008) 3088.

[9] A. Biesiekierski, J. Wang, M. A-H. Gepreel, Cuie Wen, Acta Bio 8 (2012) 5:1661.

[10] H. Kim, S. Miyazaki, Shap. Mem. Super (2016) 2:380.

[11] Z. Y. Yang, X. H. Zheng, W. Cai, Scripta Mater 99 (2015) 97.

[12] Z. Y. Yang, X. H. Zheng, W. Cai, Mater. Sci. Eng. A 655 (2016) 122.

[13] C. Y. Lei, J. S. Lee Pak, H. R. P. Inoue, C. M. Wayman, Proceedings of the International Conference on Martensitic Transformation, Monterey Institute for Advanced Studies (1992) 539.

[14] J. S. Lee Pak, C. Y. Lei, M. H. Wu, C. M. Wayman, Proceedings of the International Conference of Martensitic Transformations, Monterey Institute for Advanced Studies (1992) 533.

[15] J.S. Lee Pak, C.Y. Lei, C.M. Wayman, Mater. Sci. Eng. A 132 (1991) 237.

[16] P.J.S. Buenconsejo, H.Y. Kim, H. Hosoda, S. Miyazaki, Acta Mater 57 (2009) 1068.

[17] P.J.S. Buenconsejo, H.Y. Kim, S. Miyazaki, Scripta Mater 64 (2011) 1114.

Chapter 4

Elastocaloric effect in polycrystalline $Ni_{50}Ti_{45.3}V_{4.7}$ shape memory alloy

4.1 Introduction

Caloric materials that undergo solid to solid phase transformation on the application of various driving fields have gathered much attention as alternatives for next-generation refrigeration systems owing to their merits such as eco-friendliness, fast response, and relatively simple setup compared to the conventional vapor compression cooling [1,2]. Among them, elastocaloric (EC) materials have assessed to be the most promising candidates in a 2014 report of US Department of Energy [3]. Essentially, the EC effect is quantified by the isothermal entropy change (ΔS_{iso}) or adiabatic temperature change (ΔT_{adi}); however, it needs to evaluate various parameters related to the efficiency, e.g. the EC cooling strength, coefficient of performance (COP), and operating temperature range, to select a suitable EC material. In addition, the fatigue properties during repetitive loadings are key factors that determine long-term use in a practical application.

Shape memory alloys (SMAs) exhibiting thermal response with first-order reversible martensitic transformation (MT) by external stress have been

intensively investigated as suitable materials for the EC effect in recent years [4-8]. Although there are many classes of SMAs, depending on the chemical composition and functionality, NiTi has been a focus of interest in the research on SMAs. In view of the EC effect, NiTi shows a large temperature change (ΔT) but suffers from poor functional and structural stability [9,10]. Alloying of additional elements can help overcome this drawback. It was demonstrated that a NiTiCu film can withstand 10 million loading cycles [11] and shows a stable EC effect up to 1500 cycles without any evident degradation [12]. Additionally, a small functional fatigue effect was confirmed during thermomechanical training for NiTiCuV [13]. In a similar vein, the present work investigated the EC effect in V-added bulk NiTi. The V concentration was selected so that the SMA shows superelasticity at room temperature (RT) and low transformation thermal hysteresis (Figure 4.1) which implies good reversibility of transformation with a compatible phase boundary between the parent austenite and martensite [14].

4.2 Experimental procedure

An ingot with a nominal composition of $Ni_{50}Ti_{45.3}V_{4.7}$ (at.%) was arc-melted in an argon atmosphere using high-purity elements (99.99 wt.%). The total weight loss after seven re-melting processes was less than 0.1%. The ingot was homogenized in an evacuated quartz furnace at 1050 °C for 24 h followed by ice water quenching. Electron back scattered diffraction (EBSD) was utilized to characterize the initial microstructure of the parent austenite. The characteristic phase transformation temperatures, enthalpy change (ΔH), and specific heat capacity (C_p) were determined by differential scanning calorimetry (DSC) at a scanning rate of 10 °C min^{-1}. Before investigating the EC effect, a square prismatic specimen with dimensions of 5.0 mm × 5.0 mm × 9.0 mm was mechanically trained by 30 cyclic loadings with a compressive stress of 300 MPa at a strain rate of 0.001 s^{-1}. Subsequently, EC heating and cooling tests were performed at RT by applying and removing different stress levels in the range of 0–300 MPa at a strain rate of 0.025 s^{-1}. Each test was conducted separately. In the EC cooling test, the specimen was loaded isothermally at a strain rate of 0.0002 s^{-1} followed by holding for 5 s before unloading. The temperature of the central part of the specimen was directly monitored using an infrared thermal imaging camera. For the fatigue test, cyclic loadings were carried out with a compressive stress of 260 MPa for up to 5000

cycles with temperature monitoring at a strain rate of 0.03 s^{-1} followed by the same EC cooling test as performed on the trained specimen.

4.3 Elastocaloric effect & functional fatigue

Figure 4.2 shows the characteristics of the thermally induced reversible MT obtained by DSC measurement. The martensitic start (M_s) and finish (M_f) and austenite start (A_s) and finish (A_f) temperatures are 4.6, −6.3, 7.5, and 14.7 °C, respectively. The values of ΔH in the MT and reverse MT were estimated as −9.04 and 9.40 J g^{-1}, respectively, and corresponding entropy changes (ΔS) were calculated as −31.98 and 33.26 J Kg^{-1} K^{-1} according to the following equation,

$$\Delta S = \Delta H / T_0 \qquad (1)$$

where T_0 is the equilibrium temperature defined as $(A_f + M_s)/2$ [7]. The transformation thermal hysteresis, defined here as $(A_s + A_f - M_s - M_f)/2$= 12.0 °C, was observed to be very small compared to that of NiTi or NiTiX [15]. As mentioned above, it implies that the MT of the present SMA is highly reversible and therefore stable fatigue properties are expected. Figure 4.3 shows the inverse pole figure map of the austenite at RT for the specimen used in the EC test by EBSD. Large columnar grains perpendicular to the loading direction are observed with no specific texture development.

The compressive stress-strain (SS) curves obtained during mechanical training are shown in Figure 4.4. In the early stage of the training, plastic

deformation is evident but the final SS curve shows perfect superelasticity with complete strain recovery. The blue solid line represents the corrected SS curve of the final cycle considering the dimensional change due to plastic deformation by the training. Comparing the first and final cycles clearly demonstrates that several aspects of the superelastic behavior change gradually. The critical stress for the stress-induced MT (σ_s) decreases from 134 to 81 MPa, which can be attributed to the internal stress of dislocations generated during the training cycles [16]. The slopes of the transformation plateau in loading and unloading become steeper so that the trained SS curve is narrow with a small transformation stress hysteresis.

Figure 4.5 (a) shows the ΔT against the different applied and removed stress levels, divided into three regions— R1, R2, and R3—based on the critical stresses (σ_s and σ_f) in the loading part of the final SS curve in Figure 4.4. Interestingly, a finite ΔT is observed for R1, which can be regarded as the pure elastic part of the austenite in macroscopic scope, suggesting that a small fraction of the austenite was transformed to martensite. In R2, corresponding to the stress range of the transformation plateau, ΔT increases linearly with the stress. In R3, which is the elastic part of the transformed martensite in macroscopic scope, the stress-induced MT is almost complete. However, the small increase in the ΔT can be explained by the transformation of the remaining austenite. Using C_p (=0.51 J g^{-1} K^{-1}), the theoretical ΔT_{adi} was

estimated as 18.6 °C for the EC heating and −19.4 °C for the EC cooling according to the following equation,

$$\Delta T_{adi} = -T \cdot \Delta S / C_p \qquad (2)$$

where T is the ambient temperature. When comparing ΔT_{adi} to the measured ΔT for the largest applied and removed stress of 290 MPa, the differences seems somewhat large, which can be explained by the fact that the strain rate used for the EC test was not sufficient for the ideal adiabatic process and the transformation was not complete by 290 MPa and further loading was necessary to complete the transformation. Figure 4.5 (b) shows the corresponding strength of EC effect, $|\Delta T/\Delta\sigma|$, at the stress levels in Figure 4.5 (a). In both cases, the strengths of EC effect accomplished a maximum value slightly larger than 50 °C GPa^{-1} at the applied and removed stress of about 170 MPa, which is close to the end point of the transformation plateau. The corresponding COP values were evaluated as 11.6 for the EC heating and 22.5 for the EC cooling using the following equation,

$$COP = \Delta Q / \Delta W \qquad (3)$$

where Q is the extracted heat estimated by $C_p \cdot \Delta T$ and ΔW is the applied work

calculated by integrating the SS loop during the EC test. These values of EC cooling strength and COP are twice as large as those for NiTi wires obtained by compression [9].

Figure 4.6 (a) shows the ΔT during the fatigue test in the same time-scale, setting the minimum points of the temperature oscillation as 0. It can be seen that the decrease in the magnitude of ΔT is dominant in the first 2500 cycles. In addition, the periodic time for 1cycle decreases. This can be explained by the shortened transformation strain (ε_T) of −0.2 % shown Figure 4.6 (b), which shows the SS curves of the mechanically trained and fatigue-tested specimen. For the exact evaluation of degraded EC cooling ability, the same EC cooling test as performed on the trained specimen was carried out. Figure 4.6 (c) shows the comparison of ΔT at different removed stresses at a strain rate of 0.025 for the trained and fatigue-tested specimen. The decreased ΔT values after the fatigue test are less than 2 °C less than 20% of the initial values at all stress levels. Considering the 3 °C decrease only after 27 cycles, which is about 40% of the first value for the NiTi film [12], this result denotes an obvious improvement in the functional fatigue life.

From the EC test, it has shown that the addition of small amount of V can increases the efficiency and fatigue property of EC effect in NiTi SMA. What's the effect of V? In figure 4.1, it can be seen that the enthalpy of reverse MT, ΔH_{MA}, is decreased as the concentration of V increases so the absolute value of

Q will decrease. However, the thermal hysteresis of MT decreases that applied work for EC cycle, which is calculated by integrating the enclosed area in stress-strain curve, was decreased with the better COP value than pure NiTi. In addition, the good functional fatigue property is contributed to the enhanced compatibility of phase boundary inferred from the low hysteresis.

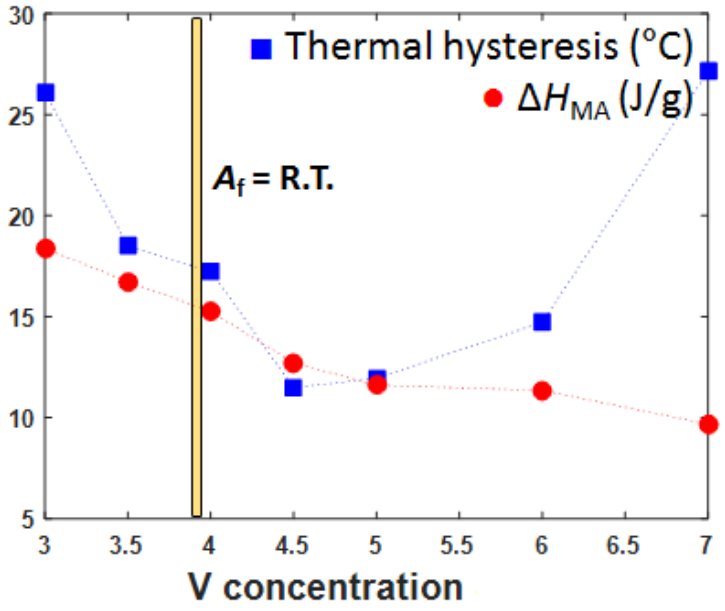

Figure 4.1 Transformation thermal hysteresis and ΔH of reverse MT as a function of V concentration (at.%).

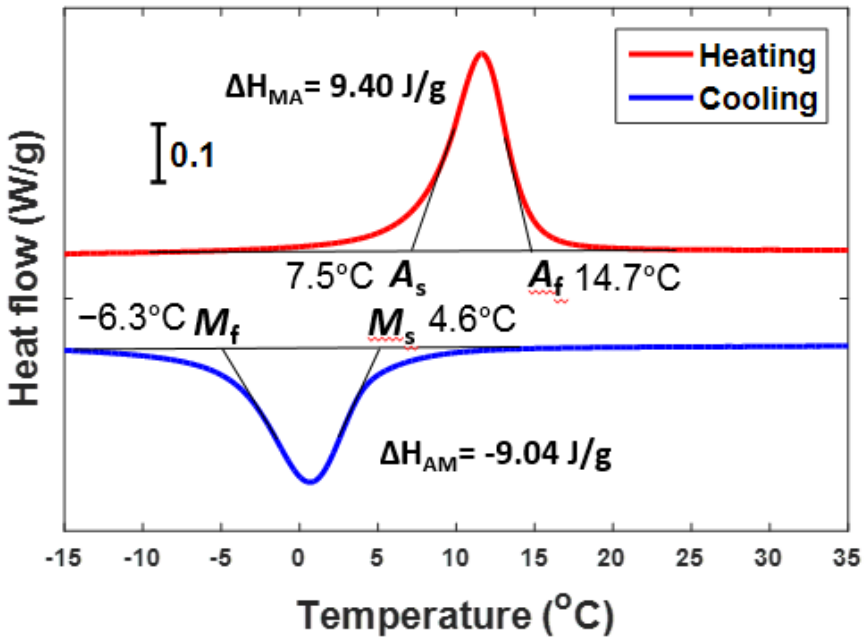

Figure 4.2 DSC curve with a scanning rate of 10 °C min^{-1}. The subscripts M and A of ΔH refer to martensite and austenite, respectively.

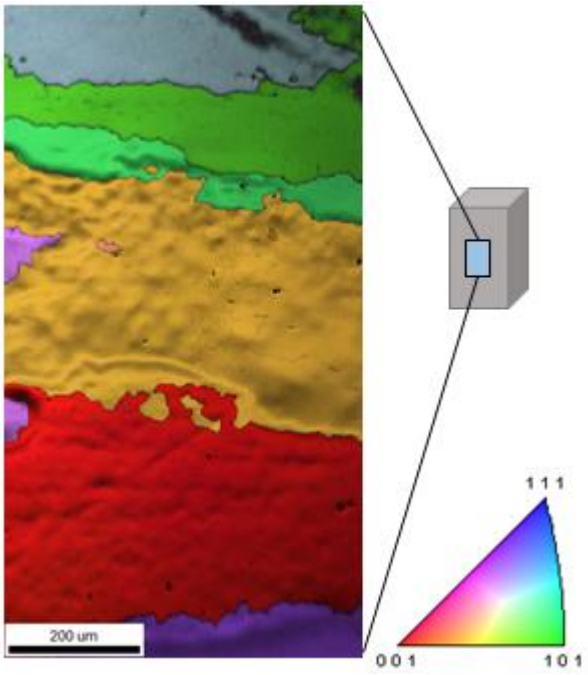

Figure 4.3 Inverse pole figure map of the austenite at RT for the specimen used in the EC test by EBSD.

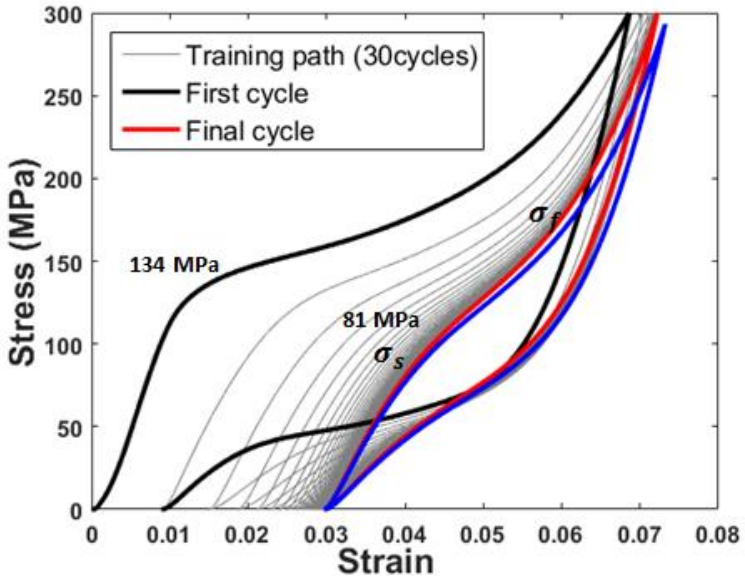

Figure 4.4 Compressive SS curves during the mechanical training of 30 cyclic loadings at RT. The blue solid line represents the corrected SS curve of the final cycle considering the dimensional change during the training.

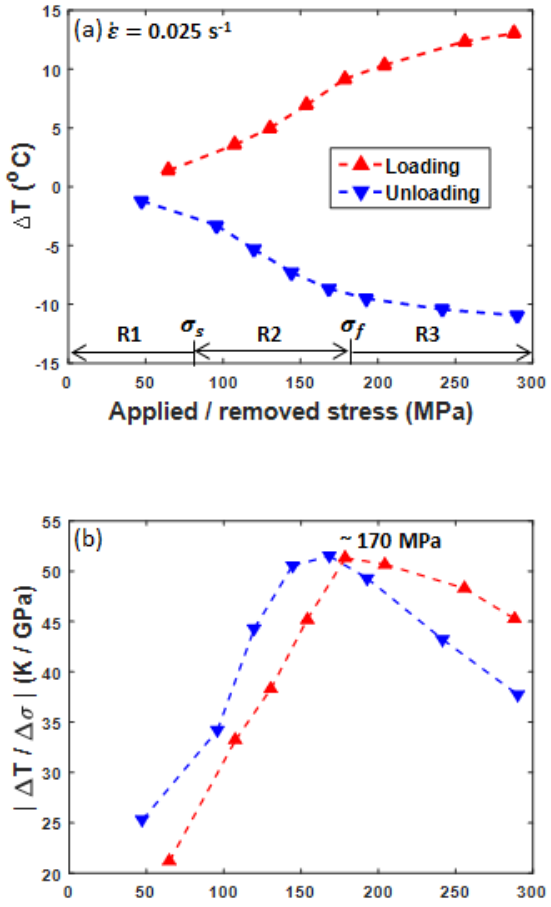

Figure 4.5 (a) ΔT against the different applied/removed stress $\Delta\sigma$ at a strain rate of 0.025 s^{-1} and (b) the corresponding strength of EC effect $|\Delta T/\Delta\sigma|$.

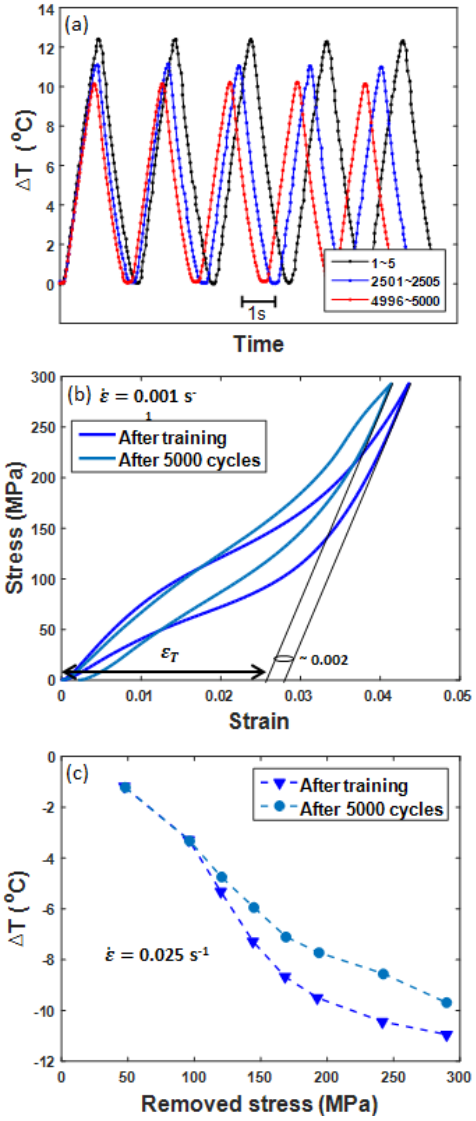

Figure 4.6 (a) ΔT against the number of cycles during the fatigue test with a compressive stress of 260 MPa at a strain rate of 0.03 s^{-1}. (b) Compressive SS curve at a strain rate of 0.001 s^{-1} and (c) ΔT as a function of removed stress $\Delta\sigma$ at a strain rate of 0.025 s^{-1} after the mechanical training and fatigue test.

4.4 Conclusion

The EC effect of $Ni_{50}Ti_{45.3}V_{4.7}$ SMA was investigated. The maximum EC cooling strength was 51.5 °C GPa^{-1} and the corresponding COP was 22.5, obtained by a removal stress of 170 MPa, corresponding to the end point of the transformation plateau. In the subsequent fatigue test of 5000 cyclic loadings, the degradation of the EC cooling power was insignificant. The present work has shown that addition of a small amount of V can enhance the efficiency and functional stability of the EC effect in NiTi.

4.5 References

[1] X. Moya, S. Kar-Narayan, D. Mathur, Nat. Mater. 13 (2014), 439.

[2] A. Chauhan, S. Patel, R. Vaish, C. R. Bowen, MRS Energy & Sustainability, (2015) 1.

[3] W. Goetzler, R. Zogg, J. Young, C. Johnson, Navigant Consulting Inc., (2014).

[4] C. Rodríguez and L. C. Brown, Metall. Trans. A 11 (1980) 147.

[5] E. Bonnot, R. Romero, L. Mañosa, E. Vives, A. Planes, Phys. Rev. Lett. 100 (2008) 125901.

[6] F. Xiao, T. Fukuda, T. Kakeshita, X. Jin, Acta Mater. 87 (2015) 8.

[7] Y. Xu, B. Lu, W. Sun, A. Yan, J. Liu, Appl. Phys. Lett. 106 (2015) 201903.

[8] A. Shen, D. Zhao, W. Sun, J. Liu, C. Li, Scrip. Mater. 127 (2017) 1.

[9] J. Cui, Y. Wu, J. Muehlbauer, Y. Hwang, R. Radermacher, S. Fackler, M. Wuttig, I. Takeuchi, Appl. Phys. Lett. 101 (2012) 073904.

[10] J. Tušek, K. Engelbrecht, L. P. Mikkelsen, N. Pryds, J. Appl. Phys. 117 (2015) 124901.

[11] C. Chluba, W. Ge, R. L. de Miranda, J. Strobel, L. Kienle, E. Quandt, M. Wuttig, Sci. 348:6238 (2015) 1004.

[12] C. Bechtold, C. Chluba, R. L. de Miranda, E. Quandt, Appl. Phys. Lett. 101 (2012) 091903

[13] M. Schmidt, J. Ullrich, A. Wieczorek, J. Frenzel, A. Schütze, G. Eggeler,

S. Seelecke, Shap. Mem. Superelasticity 1 (2015) 132.

[14] Z. Zhang, R. D. James, S. Muller, Acta Mater. 57 (2009) 4332.

[15] J. Frenzel, A. Wieczorek, I. Opahle, B. Maaß, R. Drautz, G. Eggeler, Acta Mater. 90 (2015) 213.

[16] J. Fernandez, X. M. Zhang, J. M. Guilemany, J. Mater. Porc. Tech. 139 (2003) 117.

Chapter 5

5.1 Summary

From chapter 2 through 4, several features of MT with special emphasis on crystallographic aspects including variant selection and self-accommodation and its application in different alloys were described. All MTs in those chapters fundamentally share same nature, diffusionless transformation which kinetics is independent on time term, however, many details related to MT in three cases are different. It is mainly caused by different crystal structure of the parent and product phases. For example, MT in TRIP steel in chapter 2 is irreversible and mechanically (strain) induced transformation, MT in Ti-based SMA in chapter 3 is thermally induced reversible transformation. It will be helpful to compare the details related to the general aspects of MT described in chapter 1.1 for comprehensive understanding of the present thesis. The total summary of main contents in chapter 2~4 are listed in table 5.1.

Table 5.1 Summary of main details in chapter 2~4.

	Chapter 1	**Chapter 2**	**Chapter 3**
Alloy	TRIP steel	Ti-V-Al SMA	Ni-Ti-V SMA
Driving field	Strain	Thermal quenching	Stress
Reversibility	A→M	A↔M	A↔M
Phase	A: γ (FCC) M: α' (BCC)	A: β (BCC) M: α" (orthorhombic)	A: β (BCC) M: α' (monoclinic)
Orientation relationship	$\{111\}_A$ // $\{011\}_M$ $<101>_A$ // $<111>_M$	$<011>_A$// $<010>_M$$<001>_M$ $<100>_A$ // $<100>_M$	-
Comment	**Variant selection** by **interaction E** under inhomogeneous stress state	Triangular morphology of **self-accommodation** for **minimizing macroscopic strain**	Low thermal(stress) hysteresis **Good efficiency & Functional fatigue of elastocaloric effect**
keywords	nanoindentation pop-in ASTAR KS OR FEM WLR theory interaction E variant selection	OM EBSD TEM EM theory surface trace analysis shape change self-accommodation	superelasticity thermal(stress) hysteresis training adiabatic temperature change cooling strength functional fatigue elastocaloric effect

5.2 Conclusion

Martensitic transformation (MT) in various metallic materials has been investigated for more than 100 years. Though great advances in the knowledge of martensite have been made by many researchers, fundamental understanding looks like being far away. Especially, complex microstructures of martensite in different alloys, which are the first subjects to catch up for comprehensive understanding of martensite and MT, are still puzzle. In a similar vein, the first and second parts of this thesis, respectively, deal with martensitic microstructures of the TRIP steel and Ti-based shape memory alloy (SMA) with crystallographic theories of MT. In the last part, as an effort to apply MT to real use, elastocaloric effect in V-added NiTi SMA was examined.

In first part, variant selection of mechanically induced MT in TRIP steel was investigated. A metastable austenite (γ) grain was nanoindented to introduce strain-induced MT, and multiple pop-ins, which imply transformation of the γ into martensite (α'), were detected in the nanoindentaion load-displacement curve. After the nanoindenation, cross-section of the indented region was observed using transmission electron microscope (TEM) equipped with an ASTAR system. Several martensite blocks with different variants maintaining the Kurdjumov-Sachs orientation relationship between the ex-austenite within 5 degrees were confirmed. From a finite element calculation combined with phenomenological theory for MT, it was confirmed that each

variants corresponded to those for which the transformation strain effectively accommodates external stress.

In second part, self-accommodation in Ti-V-Al SMA was studied. Exact phase information of the parent austenite and product martensite were extracted by Rietveld refinement using X-ray diffraction followed by microstructure observations using optic microscopy (OM), electron back scattered diffraction (EBSD) and TEM. The observed features of martensite microstructure including twinning mode of habit plane variants, invariant shear plane, variant clustering etc. were described with the geometrically nonlinear theory of martensite.

In third part, elastocaloric (EC) effect in polycrystalline Ni-Ti-V SMA alloy was examined. EC effect means thermal response of material respect to external uniaxial stress and have gathered much attention for the use of next-generation refrigeration systems, recently. By addition of a small amount of V (4.7 at.%), Ni-Ti-V SMA showed twice larger efficiency values such as EC cooling strength (= 50 °C GPa^{-1}) and coefficient of performance (= 22.5) than the conventional pure Ni-Ti. In addition to the efficiency improvements, the present alloy demonstrated the better functional fatigue property compared to that of pure Ni-Ti. These result can be considered as a significant progress in finding suitable materials for an application of EC.

From the present study, crystallographic aspects of MT in TRIP and SMA are detailed and described well with solid theoretical backgrounds. Moreover,

it is suggested that the newly developed alloy here can be a promising candidate for real application.

국문 초록

다양한 금속성 물질에서 나타나는 말텐사이트 변태는 100년 넘게 연구되어왔다. 말텐사이트에 관한 지식은 많은 연구자들에 의해 상당한 발전을 이뤘지만 근원적인 이해는 아직 요원하다. 특히, 말텐사이트와 그 변태에서 포괄적 이해의 핵심인 다양한 합금의 복잡한 미세조직은 여전히 풀어야 할 대상이다. 이와 같은 관점에서 본 논문의 1장과 2장은 각각 트립강과 타이타늄 기반의 형상기억합금의 말텐사이트 미세조직을 말텐사이트 변태의 결정학적 이론과 함께 다룬다. 마지막장에서는 말텐사이트 변태를 실생활에 적용하기 위해 바나듐이 첨가된 니티놀의 탄성열량효과에 대해 다룬다.

1장에서는 트립강에서 기계적으로 유기된 말텐사이트 변태의 베리언트 선택이 연구되었다. 변형 유기 말텐사이트 변태를 위해 준안정 오스테나이트에 대해 나노인덴테이션이 시행되었고, 감마상의 말텐사이트 변태를 암시하는 여러 번의 팝인이 힘-변위 그래프에서 관찰되었다. 그리고 ASTAR 시스템을 장착한 투과전자현미경을 이용해 나노인덴테이션 직하부의 단면에 대한 관찰을 수행하였다. 여러 개의 말텐사이트 블록들이 모상과

Kurdjumov-Sachs 방위관계를 5도 이하로 만족하며 생성된 것을 확인하였다. 이를 해석하기 위해 유한요소 계산과 말텐사이트 변태의 현상학적 이론을 결합하였고, 주어진 응력을 효율적으로 수용할 수 있는 변태변형을 갖는 베리언트가 선택됨을 알 수 있었다.

2장에서는 Ti-V-Al 형상기억합금의 자가수용 미세조직에 대해 연구되었다. 모상 오스테나이트와 자상 말텐사이트의 정확한 상정보를 X-ray 회절의 리트벨트 정제를 통해 추출하였고, 뒤이어 전자후방산란회절과 투과전자현미경을 통해 미세조직을 관찰하였다. 상경계면 베리언트들의 쌍정 모드, 불변 전단면 등을 말텐사이트 이론과 함께 고찰하였다.

마지막 장에서는 다결정 Ni-Ti-V 형상기억합금의 탄성열량효과에 대해 시험되었다. 탄성열량효과는 외부응력에 대한 물질의 열적 반응을 의미하며 차세대 냉각시스템의 유력한 대체후보로서 최근 많은 관심을 불러왔다. 바나듐을 소량(4.7 at.%) 첨가한 본 합금은 기존의 순수 NiTi의 2배에 해당하는 탄성열량 냉각강도(= 50 °C GPa^{-1})와 coefficient of performance (= 22.5)를 달성하였다. 이러한 효율 증가와 더불어 기능적 피로특성에서도 월등한 특성을 보였다. 이 결과는 탄성열량효과의 적용 물질을

찾는데 있어 중요한 진보라고 생각된다.

핵심어: 말텐사이트 변태, 트립강, 형상기억합금, 나노인덴테이션, 팝인, 방위관계, 말텐사이트 변태의 현상학적 이론, 유한요소법, 투과전자현미경, 베리언트 선택, 후방산란회절, 자가수용, 말텐사이트의 기하학적 비선형 이론, 탄성열량효과, 탄성열량 냉각강도, performance 계수, 기능적 피로